LIGHT METALS

Large plasticity in magnesium mediated by pyramidal dislocations

Bo-Yu Liu[1]*, Fei Liu[1]*, Nan Yang[1], Xiao-Bo Zhai[2], Lei Zhang[3], Yang Yang[4], Bin Li[4]†, Ju Li[5], Evan Ma[6], Jian-Feng Nie[7,8]†, Zhi-Wei Shan[1]†

Lightweight magnesium alloys are attractive as structural materials for improving energy efficiency in applications such as weight reduction of transportation vehicles. One major obstacle for widespread applications is the limited ductility of magnesium, which has been attributed to $\langle c+a \rangle$ dislocations failing to accommodate plastic strain. We demonstrate, using in situ transmission electron microscope mechanical testing, that $\langle c+a \rangle$ dislocations of various characters can accommodate considerable plasticity through gliding on pyramidal planes. We found that submicrometer-size magnesium samples exhibit high plasticity that is far greater than for their bulk counterparts. Small crystal size usually brings high stress, which in turn activates more $\langle c+a \rangle$ dislocations in magnesium to accommodate plasticity, leading to both high strength and good plasticity.

Magnesium is the lightest structural metal, with a density about 35% and 77% less than that of aluminum and steel, respectively (*1*). Magnesium alloys are actively being developed because of their potential usefulness for improving energy efficiency across the automobile, aircraft, and aerospace industries, in which the weight savings translate to lower energy consumption. However, the generally limited ductility of Mg at room temperature makes the processing and forming of profiles and components difficult and costly. Consequentially, low ductility has become one major obstacle that hampers the widespread applications of Mg products.

The ductility of Mg is intimately related to the fundamental behaviors of pyramidal $\langle c+a \rangle$ dislocations (fig. S1), which are the major contributor to *c*-axis strain (*2*, *3*). High ductility of Mg should therefore be achievable by generating more $\langle c+a \rangle$ dislocations (*4*–*7*). However, $\langle c+a \rangle$ dislocations are thought to be intrinsically unstable by readily transforming into sessile structures that cannot contribute to plastic strain (*8*–*10*). In light of this generally accepted understanding, proposed alloy design strategies primarily stabilize the $\langle c+a \rangle$ dislocation and prevent the glissile-to-sessile transformation (*11*). The glissile-to-sessile transformation is not observed in some recent simulation studies (*12*–*14*), in which $\langle c+a \rangle$ dislocations glide on pyramidal planes, even though the actual slip plane is under debate (*15*, *16*). Controversy surrounds the fundamental behavior of $\langle c+a \rangle$ dislocations, such as their ability to accommodate plastic strain and their slip pathways. This creates difficulties in rationalizing the mechanical behavior and for alloy design. We exploited in situ transmission electron microscope (TEM) mechanical testing (*17*, *18*), three-dimensional (3D) image reconstruction, and atomistic simulations to resolve the prevailing uncertainties. Our results document large plastic strains mediated by abundant $\langle c+a \rangle$ dislocations gliding on both pyramidal I $\{10\bar{1}1\}$ and pyramidal II $\{11\bar{2}2\}$ planes.

We performed in situ TEM mechanical testing at room temperature on submicrometer-size pillars of Mg single crystals (table S1). The pillars were fabricated by focused ion beam milling and tested inside TEM (fig. S2). We compressed the pillars along their *c* axis (Fig. 1 and movie S1), with the misalignment angle at less than 5°. In this condition, the $\langle c \rangle$ or $\langle a \rangle$ dislocation slip and $\{10\bar{1}2\}$ deformation twinning are all difficult to generate. We also conducted controlled experiments with the electron beam switched off and confirmed that the electron beam we used had no obvious effect on the mechanical behavior of the tested samples (fig. S3). We performed $\mathbf{g} \cdot \mathbf{b}$ analyses (where $\mathbf{g}$ is the diffraction vector and $\mathbf{b}$ is the Burgers vector) to determine the Burgers vector of dislocations (*19*).

All the pillars we tested underwent uniform deformation and exhibited fairly large dislocation-mediated plastic strains without failure (Fig. 1 and fig. S4). Dislocations were generated successively from the top region of the pillar, propagated gradually toward the bottom part of the pillar. With further deformation of the pillar, individual dislocations became difficult to image because their density was too high (Fig. 1C); therefore, we found it hard to analyze the Burgers vectors of these dislocations. To circumvent this difficulty, we used trapezoidal-shaped samples to generate

[1]Center for Advancing Materials Performance from the Nanoscale (CAMP-Nano) and Hysitron Applied Research Center in China (HARCC), State Key Laboratory for Mechanical Behavior of Materials, Xi'an Jiaotong University, Xi'an 710049, People's Republic of China. [2]College of Science, Xi'an University of Science and Technology, Xi'an 710054, People's Republic of China. [3]MOE Key Laboratory for Nonequilibrium Synthesis and Modulation of Condensed Matter, School of Science, Xi'an Jiaotong University, Xi'an 710049, People's Republic of China. [4]Department of Chemical and Materials Engineering, University of Nevada, Reno, NV 89557, USA. [5]Departments of Nuclear Science and Engineering and Materials Science and Engineering, Massachusetts Institute of Technology, Cambridge, MA 02139, USA. [6]Department of Materials Science and Engineering, Johns Hopkins University, Baltimore, MD 21218, USA. [7]Department of Materials Science and Engineering, Monash University, Melbourne, Victoria, 3800, Australia. [8]International Joint Laboratory for Light Alloys (Ministry of Education), College of Materials Science and Engineering, Chongqing University, Chongqing 400044, People's Republic of China.
*These authors contributed equally to this work.
†Corresponding author. Email: zwshan@xjtu.edu.cn (Z.-W.S.); jianfeng.nie@monash.edu (J.-F.N.); binl@unr.edu (B.L.)

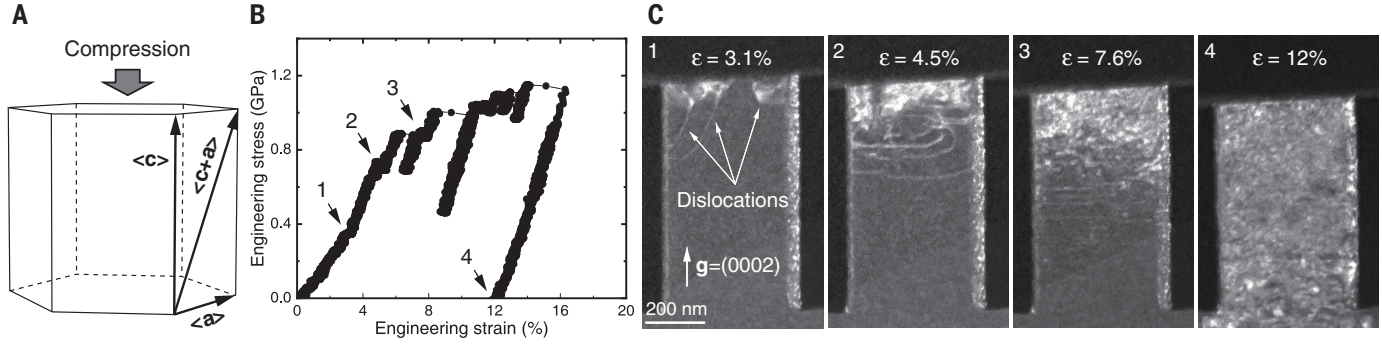

Fig. 1. In situ TEM compression test showing that dislocation slip is responsible for the plastic deformation of an Mg single-crystal pillar under *c*-axis compression. (**A**) Hexagonal unit cell showing the loading orientation. (**B**) Stress-strain curve. (**C**) Snapshots showing an increase in dislocation density during compression. The dark-field TEM observation is conducted under a two-beam condition. Electron beam direction ~$[\bar{2}110]$ (*a* axis). ε, engineering strain.

a stress gradient from the sample top to root (Fig. 2). During compression, we retracted the flat punch once dislocations appeared at the root (movie S2). Although the top was severely deformed, and its image contrast was complex, dislocations in regions near the sample root were all clearly visible. The Burgers vectors of these dislocations have both $\langle c \rangle$ and $\langle a \rangle$ components, and hence they are $\langle c + a \rangle$. Presumably, the generation and slip of the $\langle c + a \rangle$ dislocations effectively accommodates the plastic strain.

The $\langle c + a \rangle$ dislocations we observed in our study usually exhibited half-loop and zig-zag configurations (fig. S5A), similar to the $\langle c + a \rangle$ dislocations observed in bulk Mg (*4*, *20*–*22*). We believe the existence of such configurations suggests that $\langle c + a \rangle$ dislocations have both edge and screw characters and are thus of mixed type. The half loop shown in Fig. 3A formed at the top-right corner of the pillar and expanded continuously toward the lower-left corner during straining until it reached the pillar surface (fig. S6 and movie S3). This observation indicated to us that the $\langle c + a \rangle$ mixed dislocations are glissile, contributing to the plastic deformation, implying that $\langle c + a \rangle$ edge and screw dislocations are also glissile. For some $\langle c + a \rangle$ dislocations, some of their segments lie parallel to the intersection of pyramidal and basal planes and are also perpendicular to the Burgers vector. Hence, they are of edge type (see geometry analyses in fig. S5). Such edge segments are glissile (Fig. 3B and movie S4). Examination of other half loops and edge segments indicated that they are all glissile (fig. S7 and movie S5). Moreover, we observed reversible motion of $\langle c + a \rangle$ dislocations under cyclic loading (fig. S8 and movie S6). This indicates that the $\langle c + a \rangle$ dislocations retained their identity and mobility rather than becoming sessile. The mobility of the $\langle c + a \rangle$ dislocations was further supported by our atomistic simulation in which $\langle c + a \rangle$ dislocations nucleated during *c*-axis compression and glided on the pyramidal planes (figs. S9 and S10 and movie S7).

The straight segments lying parallel to the pyramidal-basal intersection were reported previously (*20*). The presence of such long segments has been attributed to low mobility of $\langle c + a \rangle$ edge dislocations (*20*), formation of sessile dislocation locks along the pyramidal-basal intersection (*23*), and dissociation of $\langle c + a \rangle$ dislocations into partials and basal stacking fault (*8*). Here, we propose that such rectilinear configuration can also result from the formation of dislocation dipole (Fig. 3C and movie S5). A straight dislocation dipole can form when a dislocation is pinned (marked by the yellow cross). The arrangement of the dipole and its two neighboring segments, 1 and 2, gave rise to an ε shape. Under the applied stress, segments 1 and 2 glided toward the left, accompanied by the elongation of the dipole. The geometry analysis indicated that this dipole was pure edge. During further straining, segments 1 and 2 formed a junction, leaving debris behind. The dislocation dipole and debris were both sessile, which can serve as obstacles to other

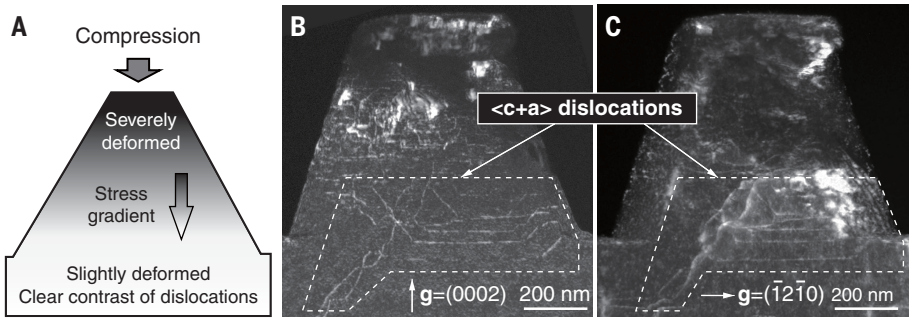

Fig. 2. Diffraction contrast analyses of $\langle c + a \rangle$ dislocations in a deformed trapezoidal sample. (**A**) Schematic illustration of the testing configuration. The pillar root is four times larger than the top. (**B** and **C**) Dark-field TEM images recorded from the same region. Electron beam direction ~[1̄010].

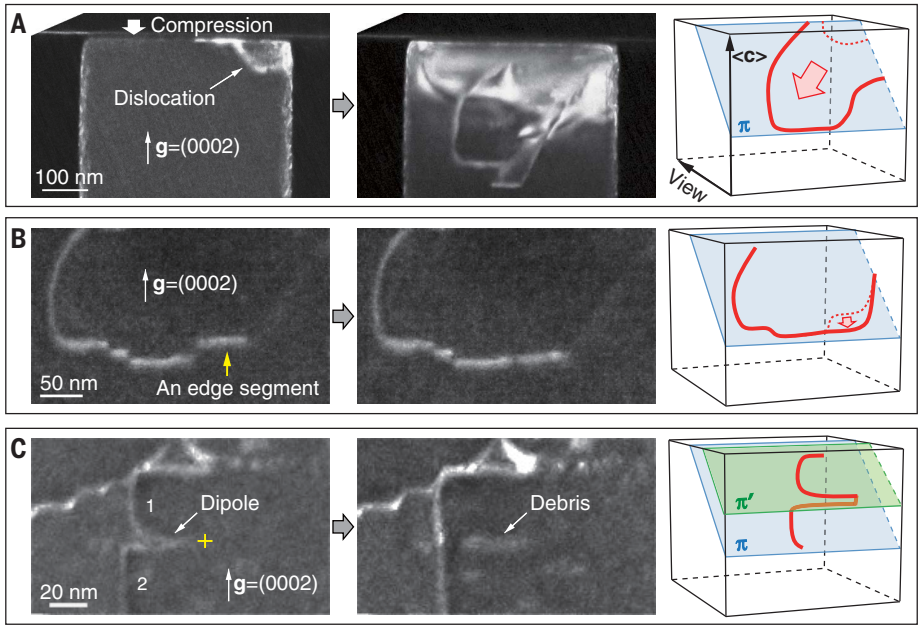

Fig. 3. In situ TEM showing the motion of $\langle c + a \rangle$ dislocations in different samples. (**A**) Expansion of a half loop. (**B**) Motion of an edge segment. (**C**) Formation of a dislocation dipole and debris. Electron beam direction ~[2̄110]. Schematic drawings of the moving dislocations are shown right to the TEM images. Symbol π refers to the pyramidal plane, and π′ is an adjacent pyramidal plane parallel to π. The red dashed line refers to the previous location of the moving dislocation.

dislocations. A likely mechanism for dipole formation by way of cross-slip is shown in fig. S11, similar to what has been proposed in other hexagonal structures such as zinc (*24*).

The formation of such a dislocation dipole requires cross-slip between two different pyramidal planes. Comparison of these two pyramidal planes is shown in fig. S12. Although the cross-slip of $\langle c + a \rangle$ dislocations between pyramidal I and II planes was studied in a computer simulation (*25*), cross-slip has not been unambiguously confirmed by experiments. Traditionally, the $\langle c + a \rangle$ slip plane is determined by slip-trace analyses, which is usually compounded by the lack of 3D information. We used a series of TEM images to construct 3D tomography to reveal the configuration and slip plane of $\langle c + a \rangle$ dislocation (fig. S13 and movies S8 and S9). Figure 4 shows 3D tomography of three $\langle c + a \rangle$ dislocations generated in *c*-axis compression. All three dislocations exhibit a curvilinear shape, indicating that they are mixed dislocations. When the pyramidal II plane is edge on, the projection of dislocation 1 becomes straight and lies on the trace of the pyramidal II plane, indicating that its gliding plane is pyramidal II (Fig. 4B). Similarly, the slip plane of dislocation 3 is pyramidal I (Fig. 4C). Dislocation 2 lies on two adjacent pyramidal II planes, indicating that cross-slip occurred. Further gliding of its segments on the two pyramidal planes would generate a dislocation dipole.

Our submicrometer-size Mg single crystals exhibit both higher strength and plasticity than

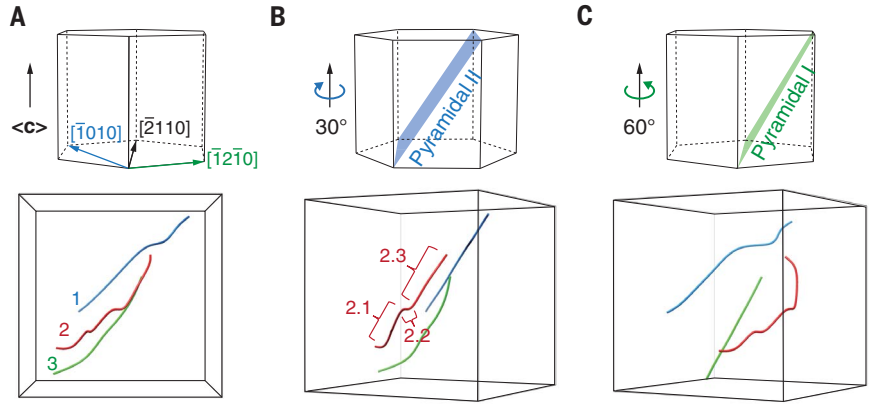

Fig. 4. 3D reconstruction revealing the pyramidal I and II gliding planes and cross-slip of $\langle c + a \rangle$ dislocations. The hexagonal unit cells indicate the viewing directions and the two pyramidal planes. (**A**) Viewing direction is [$\bar{2}$110]. Three curvilinear dislocations are selected for 3D analyses. (**B**) Viewing direction is [$\bar{1}$010]. In this orientation, the pyramidal II plane is edge on. Dislocation 1 is projected as a straight line, and hence, its slip plane is pyramidal II. For dislocation 2, segments 2.1 and 2.3 lie in different but nearby pyramidal II planes, indicating cross-slip of this dislocation. (**C**) Viewing direction is [$\bar{1}2\bar{1}0$]. The pyramidal I plane is edge on. Dislocation 3 is projected as a straight line, and therefore, its slip plane is pyramidal I.

their bulk counterpart (*26*), leading to a phenomenon of "smaller is stronger and more ductile." This phenomenon likely originates from the following factors. Small crystals usually have few preexisting dislocations, and therefore, a large amount of stress is required to nucleate dislocations. Once nucleated, dislocations can readily escape to the surfaces before dislocation multiplication, necessitating increasing stress levels to nucleate other dislocations or activate other dislocation sources to continue plasticity. Such size effects result in high stress in submicrometer-size Mg, which in turn activates abundant $\langle c + a \rangle$ dislocations to accommodate more plasticity. Another reason for the good plasticity is the rich surface sources for dislocations per unit volume, due to the large surface-to-volume ratio, which enables profuse dislocations to be generated successively from the crystal surface. Moreover, deformation twinning, which often occurs in bulk Mg under *c*-axis straining and introduces shear localization and stress concentration (*27*), is not seen in our pillars. Therefore, no potential twin-induced crack initiation sites exist in the pillars, which may also contribute to the improved plasticity. Furthermore, in a more general case, the stress concentration associated with a flaw in the tiny crystal is expected to be small, as the stress concentration factor is related to the flaw length over the flaw-tip radius. Our small crystal dimension limits this flaw aspect ratio. This prevents premature failure and allows the small crystal to maximize its potential ductility.

Our findings provide information on the mobility of pyramidal dislocations and its relationship with plasticity in pure Mg of small sizes, as well as insights into strategies for achieving long-sought plasticity in Mg that is traditionally difficult to form at room temperature. Simultaneously promoting dislocations and suppressing deformation twinning can be an effective strategy in this regard. Our experimental strategy can be extended to understanding the behavior of other hexagonal metals by identifying which microstructures promote or degrade properties such as strength and ductility.

REFERENCES AND NOTES

1. T. M. Pollock, *Science* **328**, 986–987 (2010).
2. M. H. Yoo, *Metall. Mater. Trans. A* **12**, 409–418 (1981).
3. S. Agnew, D. Brown, C. Tome, *Acta Mater.* **54**, 4841–4852 (2006).
4. S. Sandlöbes *et al.*, *Acta Mater.* **60**, 3011–3021 (2012).
5. S. Sandlöbes *et al.*, *Acta Mater.* **70**, 92–104 (2014).
6. S. R. Agnew, L. Capolungo, C. A. Calhoun, *Acta Mater.* **82**, 255–265 (2015).
7. S. Sandlöbes *et al.*, *Sci. Rep.* **7**, 10458 (2017).
8. Z. Wu, W. A. Curtin, *Nature* **526**, 62–67 (2015).
9. Z. Wu, W. A. Curtin, *Scr. Mater.* **116**, 104–107 (2016).
10. R. Ahmad, Z. Wu, S. Groh, W. A. Curtin, *Scr. Mater.* **155**, 114–118 (2018).
11. Z. Wu, R. Ahmad, B. Yin, S. Sandlöbes, W. A. Curtin, *Science* **359**, 447–452 (2018).
12. Y. Tang, J. A. El-Awady, *Acta Mater.* **71**, 319–332 (2014).
13. A. Kumar, B. M. Morrow, R. J. McCabe, I. J. Beyerlein, *Mater. Sci. Eng. A* **695**, 270–278 (2017).
14. Z. Ding *et al.*, *Acta Mater.* **146**, 265–272 (2018).
15. H. Fan, J. A. El-Awady, *Mater. Sci. Eng. A* **644**, 318–324 (2015).
16. K. Y. Xie, Z. Alam, A. Caffee, K. J. Hemker, *Scr. Mater.* **112**, 75–78 (2016).
17. B. Y. Liu *et al.*, *Nat. Commun.* **5**, 3297 (2014).
18. B.-Y. Liu *et al.*, *J. Mater. Sci. Technol.* **34**, 1061–1066 (2018).
19. Materials and methods are available as supplementary materials.
20. T. Obara, H. Yoshinga, S. Morozumi, *Acta Metall.* **21**, 845–853 (1973).
21. J. Geng, M. F. Chisholm, R. K. Mishra, K. S. Kumar, *Philos. Mag.* **95**, 3910–3932 (2015).
22. J. Jain, P. Cizek, K. Hariharan, *Scr. Mater.* **130**, 133–137 (2017).
23. B. Li, Q. W. Zhang, S. N. Mathaudhu, *Scr. Mater.* **134**, 37–41 (2017).
24. P. B. Price, *Philos. Mag.* **5**, 873–886 (1960).
25. M. Itakura, H. Kaburaki, M. Yamaguchi, T. Tsuru, *Phys. Rev. Lett.* **116**, 225501 (2016).
26. C. M. Byer, B. Li, B. Cao, K. T. Ramesh, *Scr. Mater.* **62**, 536–539 (2010).
27. M. R. Barnett, *Mater. Sci. Eng. A* **464**, 8–16 (2007).

ACKNOWLEDGMENTS

We acknowledge Z. Zhang (Hefei University of Technology) for providing the Mg single crystals; Q. J. Li (Johns Hopkins University) for fruitful discussions; and P. Zhang, C. W. Guo, and D. L. Zhang (Xi'an Jiaotong University) for assistance in focused ion beam and TEM experiments. We also appreciate the support from the International Joint Laboratory for Micro/Nano Manufacturing and Measurement Technologies and the Collaborative Innovation Center of High-End Manufacturing Equipment. **Funding:** The authors acknowledge the support from the National Key Research and Development Program of China (2017YFB0702001), National Natural Science Foundation of China (51601141, 51621063, 11504290, and 11834018), 111 Project 2.0 (BP2018008), China Postdoctoral Science Foundation (2016M600788), and the Science and Technology Department of Shaanxi Province (2016KTZDGY-04-03 and 2016KTZDGY-04-04). E.M. was supported by the U.S. Department of Energy (BES-DMSE no. DE-FG02-16ER46056). B.L. acknowledges the support from U.S. National Science Foundation (CMMI-1635088). J.-F.N. acknowledges the support from the Australian Research Council. J.L. was supported by NSF DMR-1410636. **Author contributions:** J.-F.N. and Z.-W.S. designed and supervised the project. B.-Y.L., F.L., and N.Y. performed the in situ TEM experiments and carried out the data analysis. X.-B.Z., B.-Y.L., and L.Z. carried out the 3D image reconstruction. Y.Y. and B.L. carried out the simulation and interpreted the results. J.L. and E.M. contributed to the interpretations of the observations. B.-Y.L., J.-F.N., B.L., E.M., and Z.-W.S. wrote the paper. All authors contributed to discussions of the results. **Competing interests:** The authors declare no competing interests. **Data and materials availability:** All data are available in the manuscript or the supplementary materials.

SUPPLEMENTARY MATERIALS

science.sciencemag.org/content/365/6448/73/suppl/DC1
Materials and Methods
Figs. S1 to S13
Table S1
Movies S1 to S9
References (*28*–*32*)

5 December 2018; accepted 8 May 2019
10.1126/science.aaw2843

according to their self-reported outcome of a private rolling of a die, participants, on average, report higher numbers than would be expected if they were honest, indicating that people lie, but only to a modest extent (*5*, *6*). Because participants' die rolls are private, the modest amount of lying suggests that people are concerned with maintaining a positive self-image.

Such laboratory tasks are limited by their artificial nature and by the fact that it is unclear to participants who would benefit from their honesty or suffer from their dishonesty. The question is whether such settings predict honesty outside the lab, where dishonesty often harms others. Recent work suggests that lab tasks do fairly well, revealing a positive correlation between participants' reported die roll numbers (as a proxy for dishonesty) and their tendency to free-ride on public transport (*7*) or to not return undeserved payment (*8*). Furthermore, in countries with high levels of corruption, participants report higher die roll numbers (*9*). What is still missing, however, is a direct measure for how prevalent honesty is in a natural setting, where people face varying degrees of temptation and have a clear idea of the person or group that benefits from honesty and is harmed by dishonesty.

To disentangle the influence of self-interest, self-image, and altruism in a field experiment, Cohn *et al.* handed wallets to front-desk employees at major institutions, including banks, theaters, and other public offices, claiming to have found them on the street. Each wallet contained a grocery list, a key, and three identical business cards, providing people with a way to show civic honesty by returning the wallet to its owner. To vary temptation, different amounts of money were also included in some of the wallets. Cohn *et al.* conducted many control tests and analyses to rule out the possibility that people would return the wallet out of fear of being identified or punished.

Whereas selfishness predicts that people will be less likely to return wallets containing money, altruism and the desire to maintain a positive self-image predict the opposite pattern. In 38 of the 40 countries studied, wallets with money were returned more often than wallets without money, which supports the idea that people are not purely selfish. Moreover, wallets with more money (US$94.15) were more likely to be returned than wallets with less money (US$13.45). The effect not only contradicts rational economic thinking, it is rather surprising. Both laypeople and expert economists predicted the exact opposite pattern of results in surveys reported by the authors.

Furthermore, a key is valuable to the wallet's owner, not the wallet's finder. In the United States, the United Kingdom, and Poland, the authors added an experimental treatment in which wallets included money but no key. Doing so allowed them to assess the specific contribution of altruism to honesty. Indeed, adding a key increased the likelihood of the wallet being returned. Taken together, these results support the idea that people care about others as well as caring about being honest.

Cohn *et al.*'s study provides a new way to assess human honesty. The work evokes numerous questions. By having the grocery list and business cards written in the local language, the authors identified the wallet owner as local. Our globalized world, however, is diverse. People of different ethnicities, backgrounds, and nationalities interact. Prosocial and honest behaviors are often parochial (*10*–*12*); people find it worthwhile to act kindly toward members of their own group but not members of other groups. The results reported by Cohn *et al.* may thus scale down when civic honesty is expressed toward nonlocals, including tourists or immigrants.

Also, showing civic honesty does not just mean returning a lost wallet. It is about acting in a socially desirable way, against one's selfish interests. Understanding when people are likely to engage in civic honesty—such as by whistleblowing in response to suspected organizational wrongdoing, or by obeying rules even when exposed to others' corrupt behavior—is important. By continuing to push the methodological boundaries and the proxies used to assess sensitive behaviors such as honesty, researchers aspire to figure out how to better design our environments and organizations to foster such desired behaviors. ■

REFERENCES AND NOTES

1. A. Cohn, M. A. Maréchal, D. Tannenbaum, C. L. Zünd, *Science* **365**, 70 (2019).
2. E. Fehr, K. M. Schmidt, in *Handbook of the Economics of Giving, Altruism and Reciprocity*, S.-C. Kolm, J. M. Ythier, Eds. (North-Holland, 2006), vol. 1, pp. 615–691.
3. R. Bénabou, J. Tirole, *Q. J. Econ.* **126**, 805 (2011).
4. N. Mazar, O. Amir, D. Ariely, *J. Mark. Res.* **45**, 633 (2008).
5. U. Fischbacher, F. Föllmi-Heusi, *J. Eur. Econ. Assoc.* **11**, 525 (2013).
6. P. Gerlach, K. Teodorescu, R. Hertwig, *Psychol. Bull.* **145**, 1 (2019).
7. Z. Dai, F. Galeotti, M. C. Villeval, *Manage. Sci.* **64**, 1081 (2018).
8. J. Potters, J. Stoop, *Eur. Econ. Rev.* **87**, 26 (2016).
9. S. Gächter, J. F. Schulz, *Nature* **531**, 496 (2016).
10. H. Bernhard, U. Fischbacher, E. Fehr, *Nature* **442**, 912 (2006).
11. C. K. De Dreu *et al.*, *Science* **328**, 1408 (2010).
12. S. Shalvi, C. K. W. De Dreu, *Proc. Natl. Acad. Sci. U.S.A.* **111**, 5503 (2014).

ACKNOWLEDGMENTS

This work was funded by the European Research Council (ERC-StG-637915).

Published online 20 June 2019
10.1126/science.aax5034

LIGHT METALS

Processing magnesium at room temperature

In situ microscopy experiments show how pyramidal slip increases magnesium's ductility

By **Gwénaëlle Proust**

Aluminum (Al) alloys are often used for lightweight applications such as airframes, but with proper alloying elements and heat treatments, magnesium (Mg) alloys can reach strengths comparable to those of some Al alloys but be 35% lighter (*1*). Nonetheless, the use of Mg alloys has been limited by their poor processability at room temperature and low corrosion resistance (*2*). The latter can be improved either with additional alloying elements (*2*) or by refining their grain size (*3*). Improvements to the ductility of Mg, which controls its processability, will require better understanding of its plastic deformation mechanisms and the parameters controlling their activities. On page 73 of this issue, Liu *et al.* (*4*) offer new insight into how Mg deforms, and more specifically, on the role of slip along the pyramidal planes of its unit cell in accommodating large deformation (see the figure).

> ***"The low ductility of Mg alloys is associated with their hexagonal crystalline structure."***

The potential for energy savings with lighter alloys is especially appreciated by the transportation industry (*5*). In recent years, the Volkswagen group has used around 14 kg of Mg in the Audi A4 and A6, and General Motors has used 26 kg in the GMC Savana (*6*). The forming of wrought Mg alloys—shaping them by rolling, extruding, or forging—is costly and time consuming

School of Civil Engineering, The University of Sydney, NSW 2006, Australia. Email: gwenaelle.proust@sydney.edu.au

because of the low deformation capability of these alloys at low temperatures. Shaping processes at room temperature require repeated cycles of small deformation and thermal annealing to prevent cracking. The production of bars, rods, sheets and plates at high temperatures can avoid low-temperature multiple-stage processing (*7*), but high-temperature deformation methods come with a substantial energy penalty.

Improving the ductility of Mg alloys at low temperatures would not only decrease the cost associated with their production but also would create microstructures in the alloy that could potentially improve their performance for structural applications. The low ductility of Mg alloys is associated with their hexagonal crystalline structure. Most other engineering metals are more ductile because they have a cubic crystalline structure that allows the dislocations that accommodate plastic deformation to move more readily. The structure in Mg has only limited ways for dislocations to easily glide, so deformation must be accommodated by other mechanisms, such as twinning, grain boundary sliding, and recrystallization (see the figure). The diversity of the deformation mechanisms available results in the high plastic anisotropy of Mg, which limits its ability to accommodate deformation in the directions normal to the loading direction. The deformation mechanisms that operate depend on processing parameters such as temperature, loading direction, deformation rate, and grain size (*8*, *9*).

At low temperatures, some of these mechanisms are not available, which results in cracking. Different approaches have been proposed to improve the ductility of Mg at room temperatures, including grain refinement (*10*), modification of texture (the distribution of the various crystallographic orientations present in the material) (*11*), and alloying (*12*). All these approaches aim to increase the activity of nonbasal slip (basal slip being the most favorable slip mode in Mg and its alloys); more specifically, to accommodate deformation along the *c* axis of the Mg hexagonal unit cell, $\langle c + a \rangle$ dislocations (ones that move in the direction in the unit cells that combines the $\langle c \rangle$ and $\langle a \rangle$ unit vectors) should glide on pyramidal planes.

There are actually two types of pyramidal planes in Mg: type I in the $(10\bar{1}1)$ plane and type II in the $(11\bar{2}2)$ plane. Because these two types of planes have different atomic densities, the energy required to move dislocations on them is different. To date, no consensus has been reached on which of these types of planes is prevalent during Mg deformation (*13*). The other difficulties come from studies showing contradictory results regarding the mobility of the $\langle c + a \rangle$ dislocations in pure Mg. Ahmad *et al.* stated that $\langle c + a \rangle$ dislocations are essentially sessile (immobile) but that this problem can be overcome with proper alloying (*14*). Kumar *et al.* showed that although $\langle c + a \rangle$ dislocations on pyramidal type I planes become sessile, the ones on pyramidal type II planes remain glissile under stress (*15*).

Liu *et al.* present results related to both controversies. They used advanced in situ transmission electron microscopy (TEM) mechanical testing techniques to apply a compressive load at room temperature on Mg micropillars fabricated from single crystals. Both pyramidal type I and pyramidal type II planes participate to plastically deform Mg. Their recording of the visualized deformation synchronized with the mechanical response of the material showed unequivocally the relation between strain accommodation and the formation and motion of $\langle c + a \rangle$ dislocations. They also used three-dimensional reconstruction techniques on the TEM images captured at different tilting angles to identify the planes (pyramidal type I or II) on which different dislocations are lying and to even identify dislocation cross-slip. The glissile character of the dislocations is confirmed on both types of pyramidal planes by molecular dynamics simulations in which $\langle c + a \rangle$ dislocations nucleate because of compressive loading along the *c* axis, instead of by being artificially introduced in the model. The reversibility of dislocation motion is demonstrated through cyclic loading observed during in situ TEM testing.

The findings of Liu *et al.* reinforce the idea that promoting $\langle c + a \rangle$ dislocation activity in Mg can increase its processability. Using the proposed molecular dynamics model, it will become possible to identify microstructures that are favorable to increase ductility in Mg and its alloys at room temperature. The combined experimental and modeling approach used in this study can be repeated on different Mg alloys to confirm and better understand the role of alloying elements in the ductility of Mg, which will allow the development of new wrought Mg alloys. ■

Mapping magnesium deformation

Atoms in magnesium accommodate strain through several mechanisms when the metal is deformed. Liu *et al.* studied one mechanism, slip along pyramidal planes, with electron microscopy while the metal was strained.

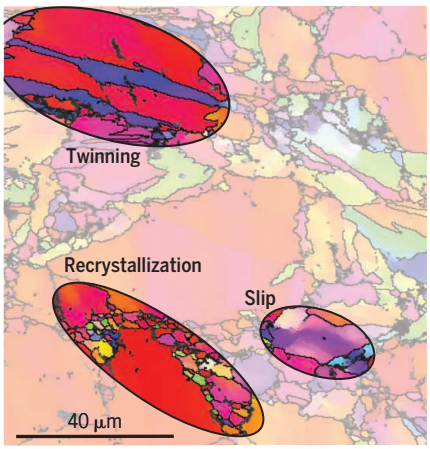

Accommodating strain Changes in microstructure characterized with electron backscatter diffraction that resulted from straining a magnesium alloy are shown as changes in color and smaller grains. Three different mechanisms—slip, twinning, and recrystallization—simultaneously accommodate strain in this sample.

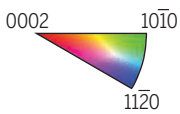

Packing atoms

Two families of pyramidal planes can accommodate deformation in this hexagonal close-packed metal.

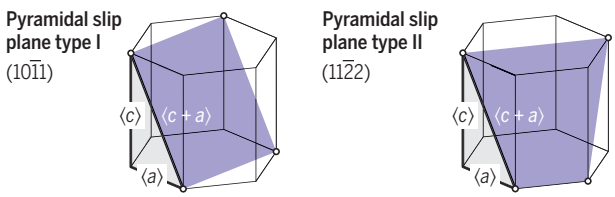

REFERENCES AND NOTES

1. I. Polmear, D. StJohn, J.-F. Nie, M. Qian, Ma, *Light Alloys - Metallurgy of the Light Metals* (Elsevier, ed. 5, 2017).
2. W. Xu *et al.*, *Nat. Mater.* **14**, 1229 (2015).
3. D. Song *et al.*, *Mater. Des.* **166**, 107621 (2019).
4. B.-Y. Liu *et al.*, *Science* **365**, 73 (2019).
5. T. M. Pollock, *Science* **328**, 986 (2010).
6. D. Sameer Kumar, C. Tara Sasanka, K. Ravindra, K. N. S. Suman, *Am. J. Mater. Sci. Technol.* **4**, 12 (2015).
7. C. Moosbrugger, L. Marquard, *Engineering Properties of Magnesium Alloys* (ASM International, 2017).
8. S. R. Agnew, O. Duygulu, *Int. J. Plast.* **21**, 1161 (2005).
9. M. W. Vaughan *et al.*, *Acta Mater.* **168**, 448 (2019).
10. P. Lukáč, Z. Trojanová *Mater. Eng. Mater. Inž.* **18**, 111 (2011).
11. E. Dogan, M. W. Vaughan, S. J. Wang, I. Karaman, G. Proust, *Acta Mater.* **89**, 408 (2015).
12. Z. Wu, R. Ahmad, B. Yin, S. Sandlöbes, W. A. Curtin, *Science* **359**, 447 (2018).
13. Z. Ding *et al.*, *Acta Mater.* **146**, 265 (2018).
14. R. Ahmad, B. Yin, Z. Wu, W. A. Curtin, *Acta Mater.* **172**, 161 (2019).
15. A. Kumar, B. M. Morrow, R. J. McCabe, I. J. Beyerlein, *Mater. Sci. Eng. A* **695**, 270 (2017).

ACKNOWLEDGMENTS

I thank I. Karaman and his team at Texas A&M University for the Mg specimen used to illustrate the article and acknowledge Microscopy Australia for use of the microscopy characterization equipment at the Australian Centre for Microscopy and Microanalysis at the University of Sydney.

SUPPLEMENTARY MATERIALS

science.sciencemag.org/content/365/6448/30/suppl/DC1

10.1126/science.aax9732

GRAPHIC: A. KITTERMAN/*SCIENCE*

science.sciencemag.org/content/365/6448/73/suppl/DC1

Supplementary Materials for

Large plasticity in magnesium mediated by pyramidal dislocations

Bo-Yu Liu*, Fei Liu*, Nan Yang, Xiao-Bo Zhai, Lei Zhang, Yang Yang, Bin Li†, Ju Li, Evan Ma, Jian-Feng Nie†, Zhi-Wei Shan†

*These authors contributed equally to this work.
†Corresponding authors. Email: binl@unr.edu (B.L.); jianfeng.nie@monash.edu (J.-F.N.); zwshan@xjtu.edu.cn (Z.-W.S.)

Published 5 July 2019, *Science* **365**, 73 (2019)
DOI: 10.1126/science.aaw2843

This PDF file includes:

Materials and Methods
Figs. S1 to S5
Table S1
Captions for Movies S1 to S9
References

Other Supplementary Materials for this manuscript include the following:
(available at science.sciencemag.org/content/365/6448/73/suppl/DC1)

Movies S1 to S9

Materials and Methods

Sample fabrication

Sample fabrication and annealing procedures are schematically illustrated in fig. S2. The pure Mg single crystal was grown using the Bridgman method under Ar protection. Millimeter-sized pieces were cut from the bulk samples using electrical discharge machining, with one edge lying parallel to the [0001] orientation. These pieces were ground into thin slices with a thickness of ~100 μm. One side of the sample was thinned by twin-jet electro-polishing to a wedge shape with the thin edge of ~10 μm.

Sub-micron pillars were fabricated from the thin edge using FIB (Ga^+ sources, 30 kV and low ion current (several to tens of pA)). The cross-section of the pillar had a square shape (see detailed geometrical parameters in table S1). The cutting angles were set up in such a way that the pillars had a negligible taper angle (Fig. 1), or a trapezoidal shape (Fig. 2). To minimize ion-beam irradiation damage, the pillars were fabricated via glancing milling on the lateral surface, such that direct irradiation on the pillar surface can be minimized. A low energy ion-beam (5 kV, 1.5 pA) was then used to clean the pillar surface to reduce the thickness of damaged layer. Nevertheless, defects could still be induced at the pillar surface during FIB milling, which would degrade the imaging quality, sometimes even fog the dislocations. To remove these FIB-induced defects on sample surface, the pillars were annealed at ~180 °C for ~15 min, inside a tube furnace in an Ar atmosphere.

In-situ mechanical testing

The in-situ mechanical testing at room temperature was performed on a Hysitron PicoIndenter (PI95, fig. S2) inside a JEOL 2100F TEM and a Hitachi H-9500 ETEM. Gatan 833 camera and Gatan OneView camera were used to record the in-situ movie inside JEOL 2100 TEM and H-9500 ETEM, respectively. The mechanical loading was conducted under displacement control. The strain rate was in the level of 10^{-3} s^{-1}.

The pillars were compressed by a diamond flat punch. The punch surface and the pillar top surface are generally not perfectly parallel to each other. Therefore, pillar can occasionally be slightly curved during loading.

The $\boldsymbol{g}\cdot\boldsymbol{b}$ analyses to determine the Burgers vector

We chose $\boldsymbol{g}=(0002)$ and $\boldsymbol{g}=(\bar{1}2\bar{1}0)$ beams for dark-field imaging in the present work. $\boldsymbol{b}$ is the Burgers vector of the dislocation. Based on the $\boldsymbol{g}\cdot\boldsymbol{b}$ invisibility criterion, only $\langle c+a\rangle$ dislocation is visible in the dark-field images obtained with $\boldsymbol{g}=(0002)$ and with $\boldsymbol{g}=(\bar{1}2\bar{1}0)$. $\langle a\rangle$ dislocation is invisible when $\boldsymbol{g}=(0002)$, and $\langle c\rangle$ dislocation is invisible when $\boldsymbol{g}=(\bar{1}2\bar{1}0)$.

3D image reconstruction

A series of electron tomography images were acquired from large angle tilting between -33° and +33°, with 1° difference between two adjacent tilting angles. These images were aligned by the IMOD software (*28*) (https://bio3d.colorado.edu/imod/), then used to construct 3D tomography of the dislocations in these images. The 3D reconstructed dislocation was visualized by using UCSF Chimera (*29*) (http://www.rbvi.ucsf.edu/chimera).

Molecular dynamics simulation

The modified embedded atom method (MEAM) potential developed by Wu and Curtin (*8*) was used to simulate the formation and glide of pyramidal $\langle c+a\rangle$ dislocations in single crystal

Mg. The system contained 2112000 atoms with dimensions 53×34×27 nm. Free surfaces were applied to all three dimensions. The system was compressed by displacing atoms on one of the free surfaces along the *c*-axis at a constant rate, corresponding to a strain rate of 1.9×10^{8} /sec. The temperature of the system was maintained at 300 K by using the Nosé–Hoover thermostat. No dislocation was artificially introduced before loading, and all $\langle c+a \rangle$ dislocations were produced by the compressive loading.

Fig. S1.

Schematic of $\langle c + a \rangle$ edge, screw and mixed dislocations and their motions on the pyramidal plane (π). The line direction of a pure edge or screw dislocation is perpendicular or parallel to the $\langle c + a \rangle$ Burgers vector. The mixed dislocation is neither perpendicular nor parallel to the $\langle c + a \rangle$ Burgers vector. Therefore, if a dislocation line is curved, it must be a mixed dislocation containing both edge and screw components. Gliding of a mixed dislocation (or the expansion of a loop) requires the motion of both edge and screw components or segments.

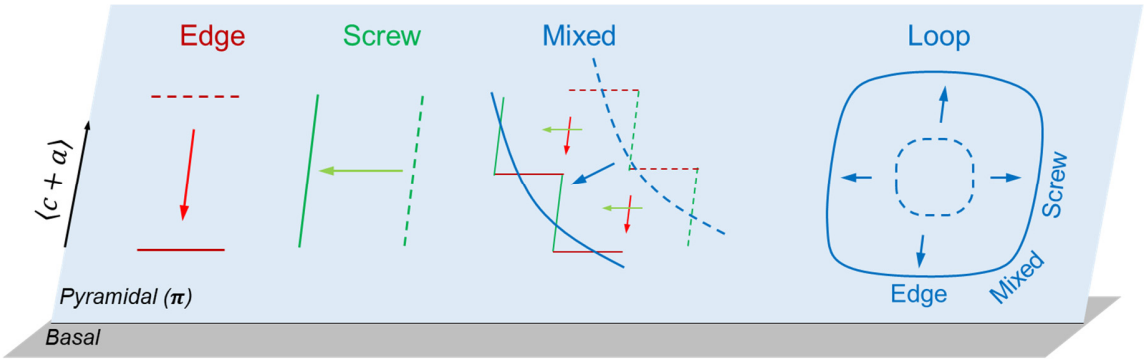

Fig. S2.

Sample fabrication and loading setup. (A) Pre-machining. The [0001] orientation is marked by the red arrow. (B) Sub-micron pillars were fabricated by FIB. The pillars were then annealed to remove FIB-induced defects on pillar surface. (C) The sample was mounted on a Hysitron PicoIndenter (PI95) holder to perform in-situ TEM mechanical testing. The pillar was compressed by a diamond indenter with a flat punch.

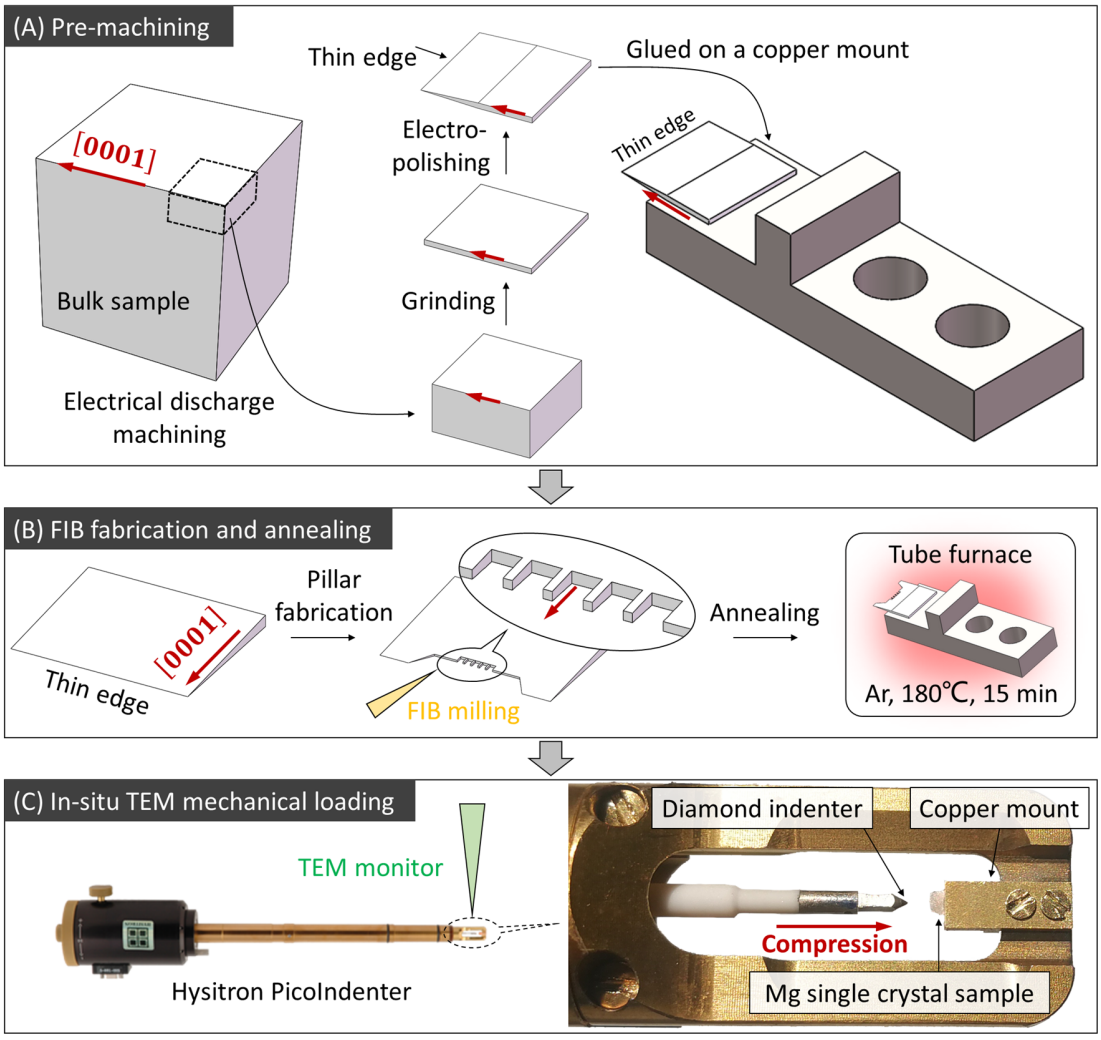

Fig. S3.

Comparison of compression tests with electron beam switched on and off indicates that the electron beam is not responsible for the observed dislocation slip mediated plasticity. The two pillars were fabricated from the same Mg single crystal, using the same FIB milling and annealing parameters. Dark-field TEM images of the initial and deformed pillar showing that plastic deformation had occurred with electron beam on (A), and with electron beam off (B). Electron beam direction ~$[\bar{2}110]$. (C) Corresponding mechanical data. These two pillars exhibited similar shape change after plastic deformation. Both contained large numbers of dislocations. The force-displacement curves of these two tests show no significant difference. Since the programmed displacement in beam-on test was slightly larger than that in beam-off test, larger final plastic strain and higher dislocation density were generated in the beam-on pillar. In the severely deformed area (red dashed frames), the dislocation density in the beam-off pillar was almost as high as that in the beam-on pillar.

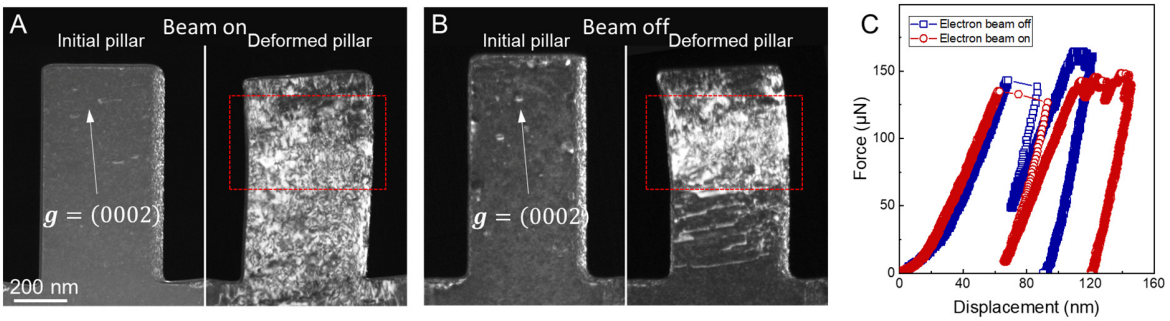

Fig. S4.

SEM images of a pillar before and after compression showing uniform plastic deformation along the loading direction (*c*-axis). Inset, schematic of hexagonal unit cell showing the initial orientation of the pillar. The compression direction and pillar thickness direction are approximately parallel to *c*-axis and *a*-axis, respectively. Selected area electron diffraction patterns acquired across the entire sample indicate the absence of deformation twinning.

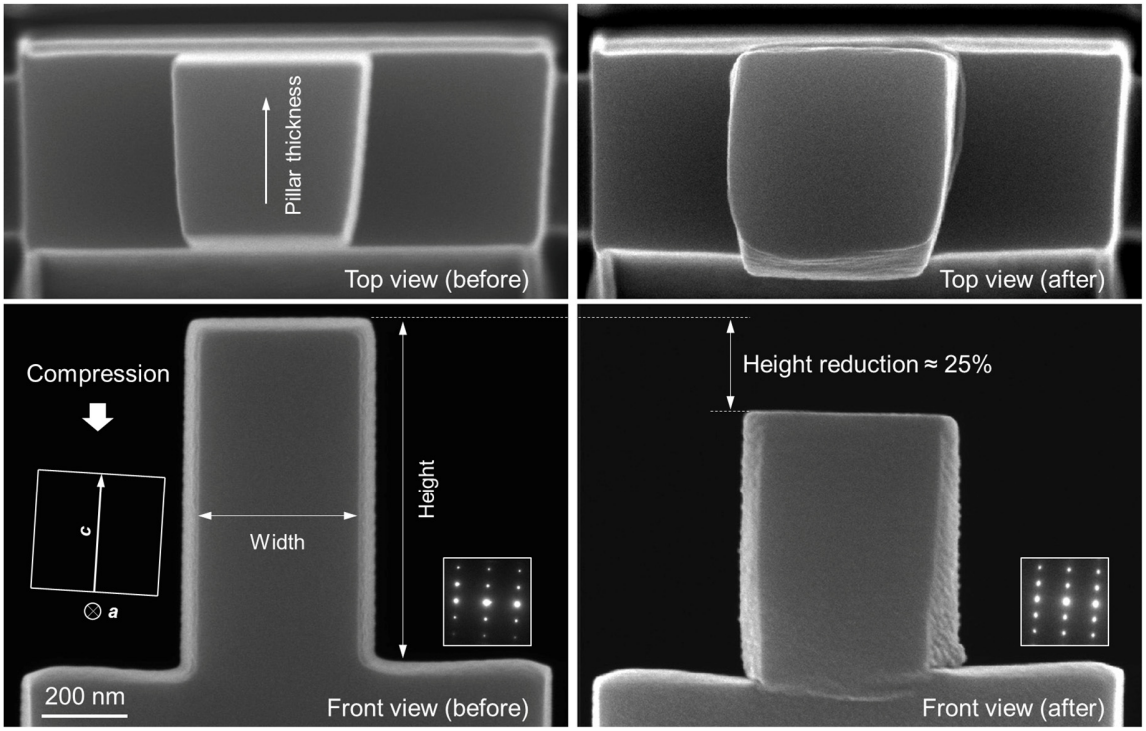

Fig. S5.

Determination of edge and mixed dislocations. (A) Schematic of dislocation half-loops and a dislocation with a zig-zag shape. (B) Dark-field TEM images of $\langle c+a \rangle$ dislocations (Fig. 2) viewed along $[\bar{1}010]$ and $[\bar{2}110]$. Parts of individual dislocations are along the horizontal direction of the figure (parallel to the basal plane), while other segments are inclined. (C) Intersection line (green line, along $\langle \bar{1}100 \rangle$) of basal and pyramidal planes is perpendicular to $\langle 11\bar{2}3 \rangle$ (red). Therefore, the dislocation along the intersection line of basal and pyramidal planes should be of edge type. (D) Projections of $\langle 11\bar{2}3 \rangle$ directions along $[\bar{1}010]$ and $[\bar{2}110]$, respectively. For a pure screw dislocation, it should be a straight line along $\langle 11\bar{2}3 \rangle$ orientation. However, angles between the dislocation lines and the basal trace shown in (B) are not equal to the angles given in (D), indicating that these inclined segments are of mixed type.

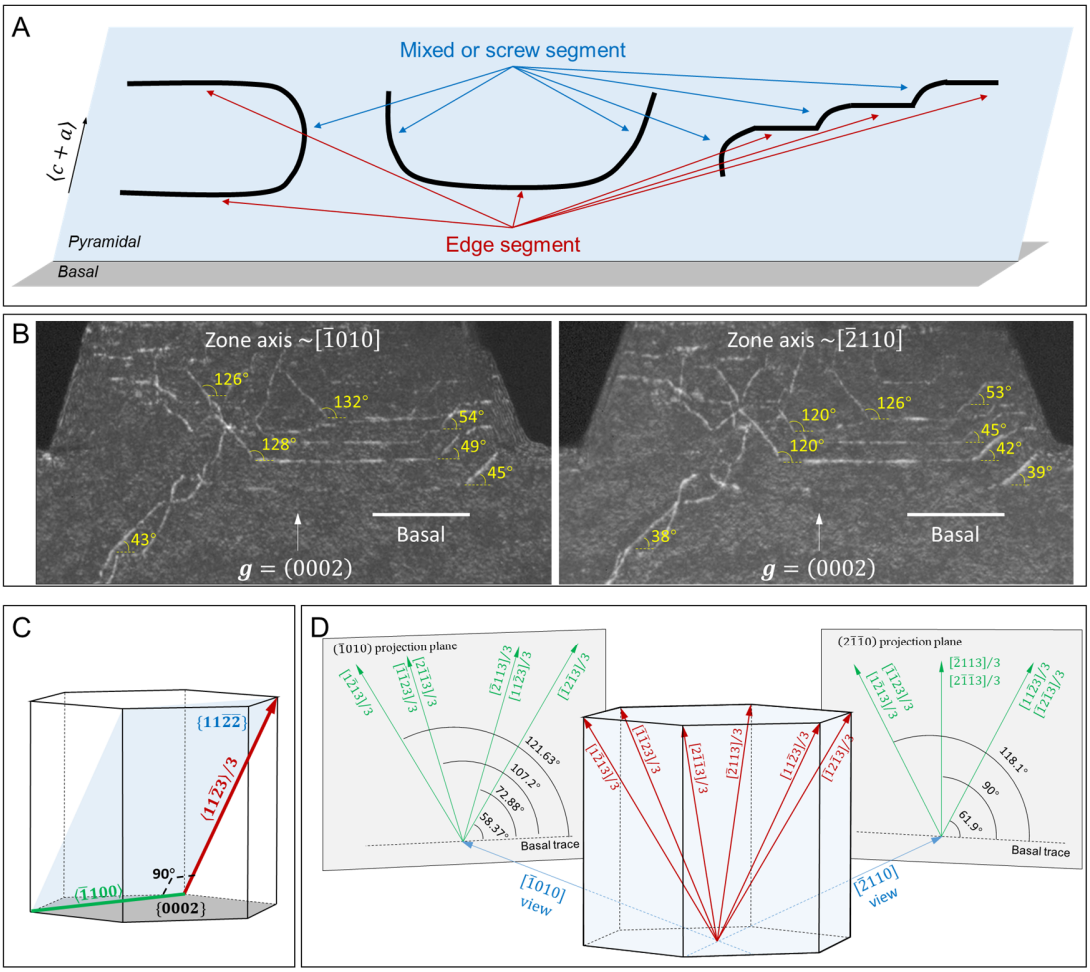

Fig. S6.

In-situ TEM observation of the expansion of a dislocation half-loop (Fig. 3A). (A) The dislocation half-loop formed at top-right-corner. (B) The loop expanded towards lower-left. Part of the dislocation moved to near the surface, but blocked by the surface oxide layer, forming a straight line (yellow arrow) along the intersection of surface and slip plane. (C-D) The loop laterally expanded. Similarly, the left part of the dislocation was blocked near the left surface (yellow arrow). Electron beam direction ~$[\bar{2}110]$.

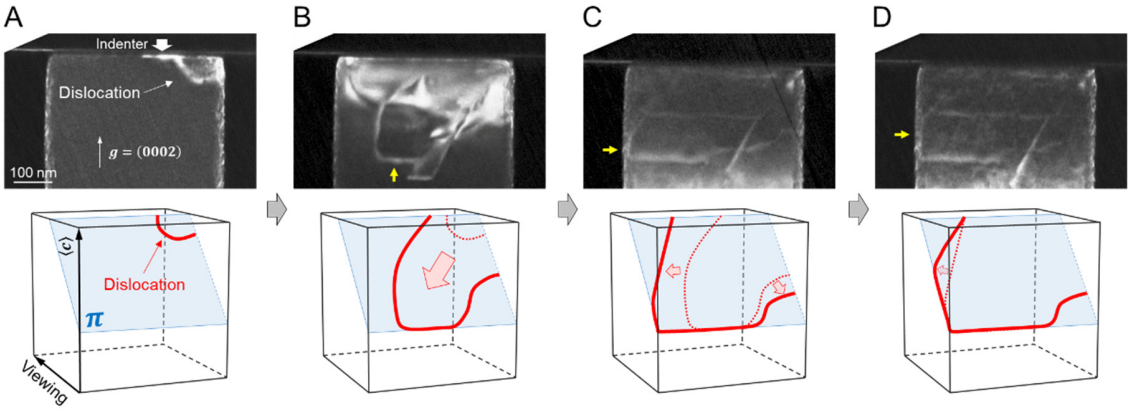

Fig. S7.

In-situ TEM observation of the expansion of two dislocation half-loops and the motion of their edge segments. The initial position of these two dislocations are marked by yellow triangles. Schematic drawings of the moving dislocations are shown below the TEM images. The two dislocations are displayed by red and blue colors, respectively. Dashed lines indicate the previous locations of the gliding dislocations. Electron beam direction ~$[\bar{2}110]$. The edge segment seems to have low mobility, but it might be due to the pinning effect of other dislocations.

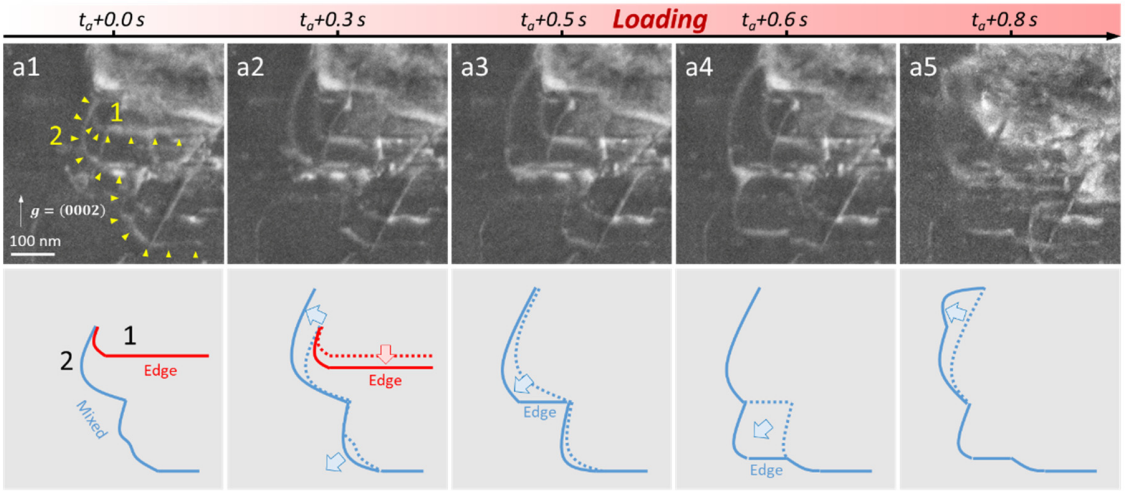

Fig. S8.

Reversible motion of a $\langle c + a \rangle$ dislocation under cyclic loading. The dislocation glided leftwards during first loading, retracted back during unloading, glided leftwards again during second loading, and then retraced back during the second unloading. Schematic drawings of the moving dislocations are shown below the TEM images. Red dashed lines indicate the previous locations of the gliding dislocation. Electron beam direction ~$[\bar{2}110]$.

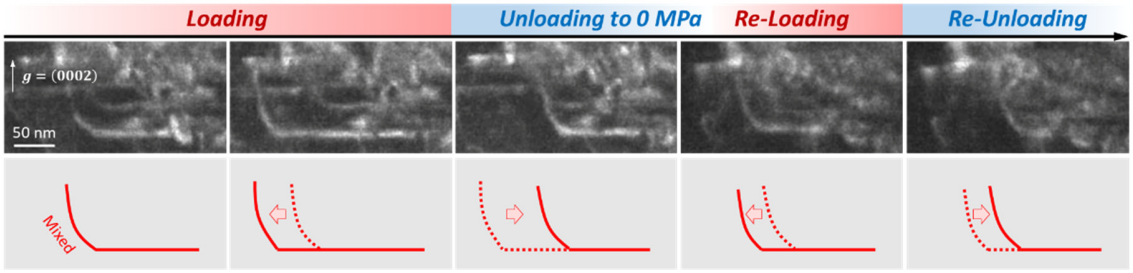

Fig. S9.

Molecular dynamics simulation showing the formation and glide of $\langle c + a \rangle$ dislocations in time sequence during *c*-axis compression of a Mg single crystal. Common neighbor analysis was used to detect the defects. Atoms of the hexagonal structure and on the surface are hidden to show only dislocation lines and stacking faults (SFs). Multiple $\langle c + a \rangle$ dislocations were generated near the corners, then glided on pyramidal I and II planes. In each of these dislocation formation events, a leading partial formed first, creating a pyramidal SF, followed by the formation of a trailing partial that erased the SF, which is similar to those reported in a previous simulation study (*12*). Red dashed lines are drawn to schematically show the position of partials. Dislocations on intersecting pyramidal planes formed sessile junctions.

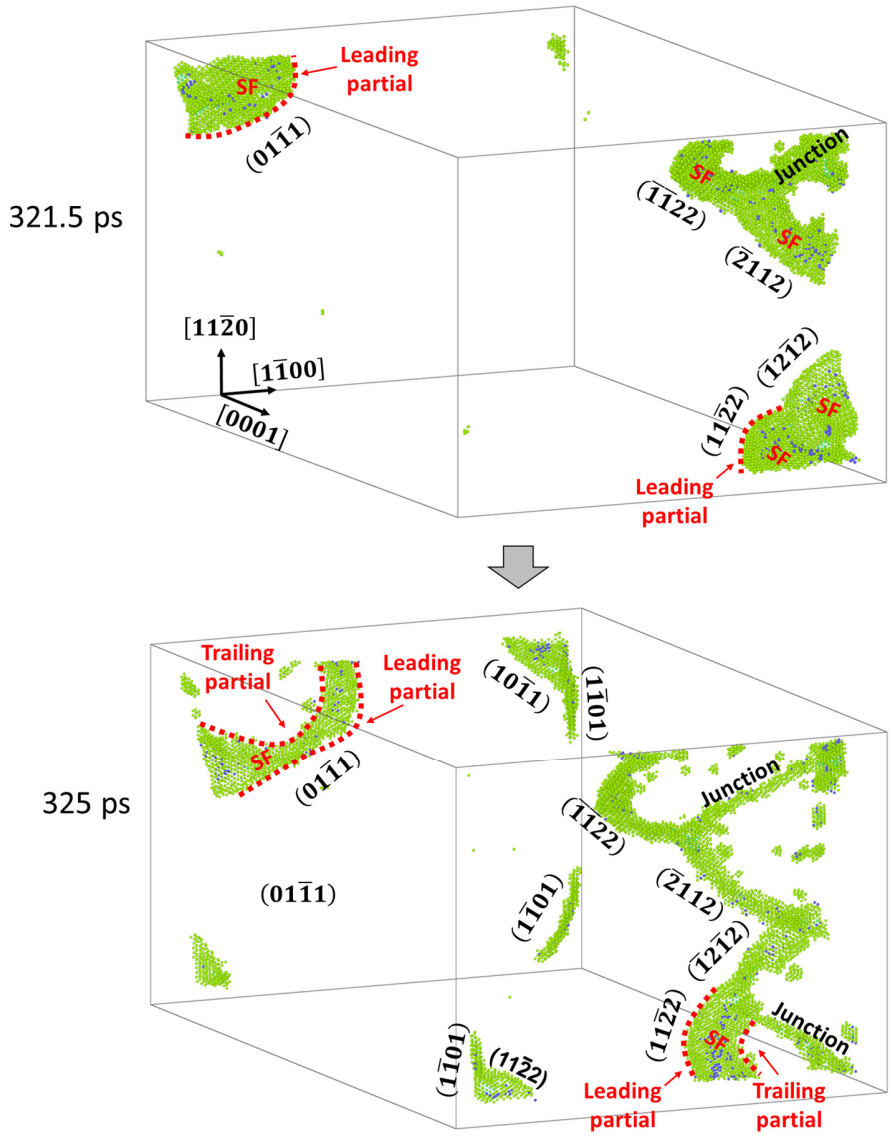

Fig. S10.

Burgers vector analysis of $\langle c+a \rangle$ dislocation generated by deformation. The basal planes are colored alternately in yellow and green to better reveal the dislocation structure. (A) The core structure of an edge segment of a mixed pyramidal II $\langle c+a \rangle$ dislocation. This dislocation comprises a leading partial and a trailing partial that are separated by a SF (dotted red line) in the gliding pyramidal II plane. The Burgers vector is $\frac{1}{3}[\bar{1}\bar{1}23]$, i.e. $\langle c+a \rangle$. (B) The core structure of a mixed pyramidal I $\langle c+a \rangle$ dislocation. It also comprises a leading partial and a trailing partial separated by a SF (dotted red line). The Burgers vector shown by the circuit is $\frac{1}{2}[1\bar{1}0\bar{2}]$. The $\frac{1}{6}[\bar{1}\bar{1}20]$ component of the trailing partial of this dislocation cannot be seen when viewed along $[\bar{1}\bar{1}20]$. The total Burgers vector is $\frac{1}{2}[1\bar{1}0\bar{2}]+\frac{1}{6}[\bar{1}\bar{1}20]=\frac{1}{3}[1\bar{2}1\bar{3}]$, i.e. $\langle c+a \rangle$. The "leading partial + pyramidal SF + trailing partial" structure is similar to those reported in a previous simulation study (*12*) using two different potentials developed by Liu et al. (*30*) and Sun et al. (*31*). The $\langle c+a \rangle$ dislocations formed during plastic deformation, at least under our simulation conditions, do not transform into sessile structures (on the basal plane) that evolve from artificially-introduced $\langle c+a \rangle$ dislocations (*8*).

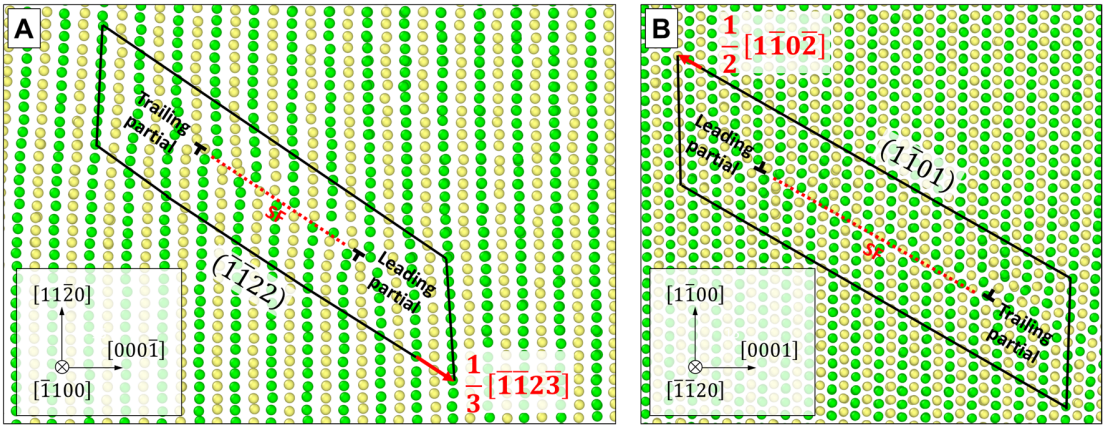

Fig. S11.

Schematic diagrams illustrating the formation of dislocation dipole and sessile loop through cross-slip. (A) $\langle c+a \rangle$ Burgers vector shared by three pyramidal planes, $(1\bar{2}12)$ marked by π, $(01\bar{1}\bar{1})$ marked by π^* and $(1\bar{1}01)$ marked by π^{**}. (B) A screw dislocation glides leftwards on π. Part of the dislocation (segment 1) cross-slips onto π^*, while the segment 2 still glides on π. Two edge segments form by this process. (C) The segment 1 cross-slips from π^* to π' (π' is an adjacent $(1\bar{2}12)$ plane parallel to π), generating an edge dislocation dipole. (D) As the segments 1 and 2 glide leftwards on π and π' respectively, the dipole elongates. (E) The segment 1 cross-slips from π' to π^{**} then to π, and joints segment 2. The dipole now closes into a loop. The loop is normal to the $\langle c+a \rangle$ Burgers vector, so it is sessile.

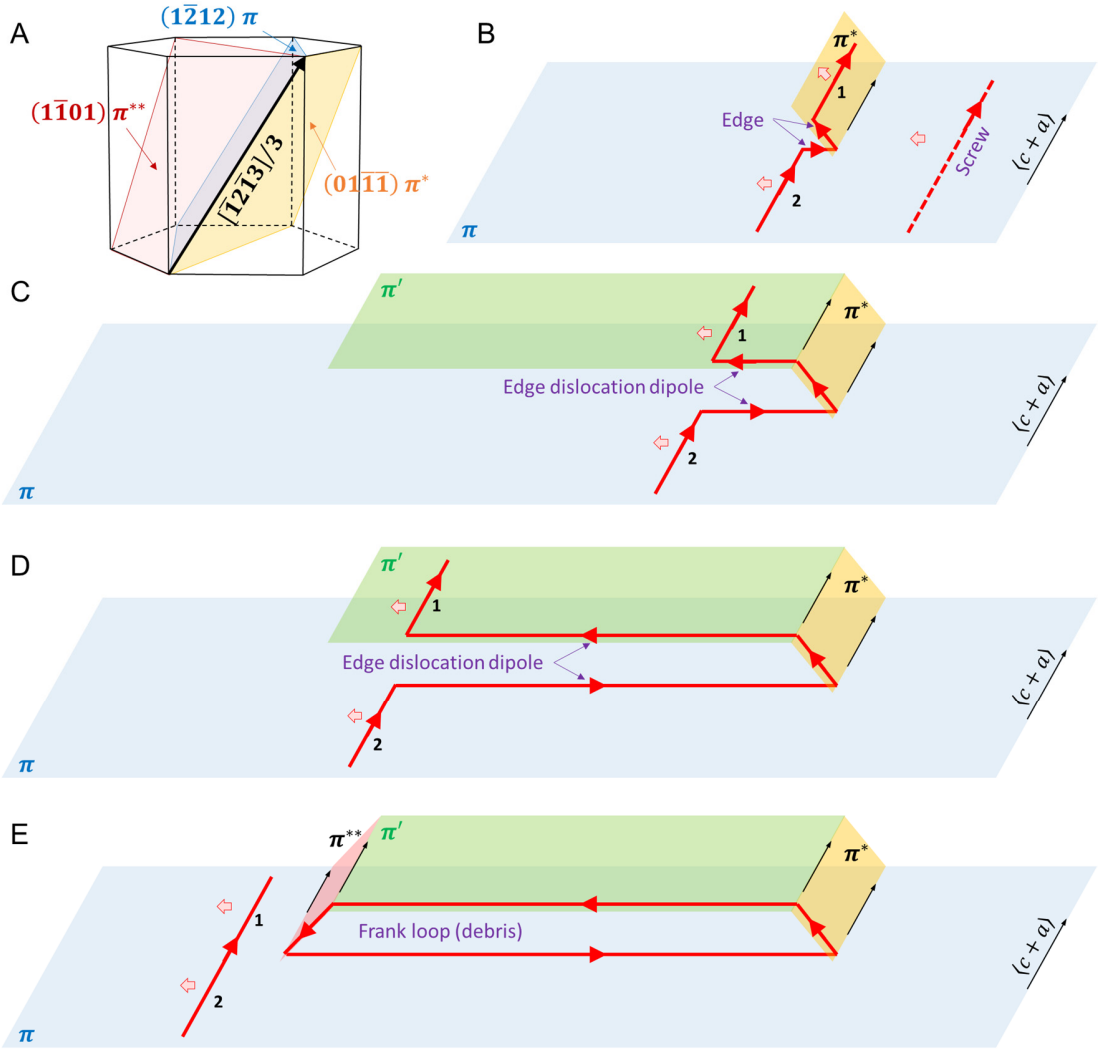

Fig. S12.

Comparison of two pyramidal slip planes. (A) Hexagonal unit cells viewed along $\langle \bar{1}2\bar{1}0 \rangle$ (right) and $\langle 0\bar{1}10 \rangle$ (left) showing the edge-on view of pyramidal I and II planes. (B) Packing of atoms in pyramidal I (green) and II (blue) planes. The pyramidal I plane is rugged. Atoms in alternating planes are distinguished by dark and light green colors. The intersecting line of these two planes is $\langle c + a \rangle$ (red). The pyramidal I plane has a higher atomic packing density than pyramidal II plane ($\rho_{\{10\bar{1}1\}} \approx 10.63$ atoms$/nm^2$, $\rho_{\{11\bar{2}2\}} \approx 5.94$ atoms$/nm^2$). The Peierls stress for the pyramidal II $\langle c + a \rangle$ slip should be higher than the pyramidal I $\langle c + a \rangle$ slip ($\tau_{PN} \propto Ge^{-2\pi d/(1-\nu)b}$, where d is interplanar spacing, G is shear modulus, ν is Poisson's ratio, b is the magnitude of Burgers vector (*32*)). The difference may be offset by the fact that the pyramidal I plane is corrugated.

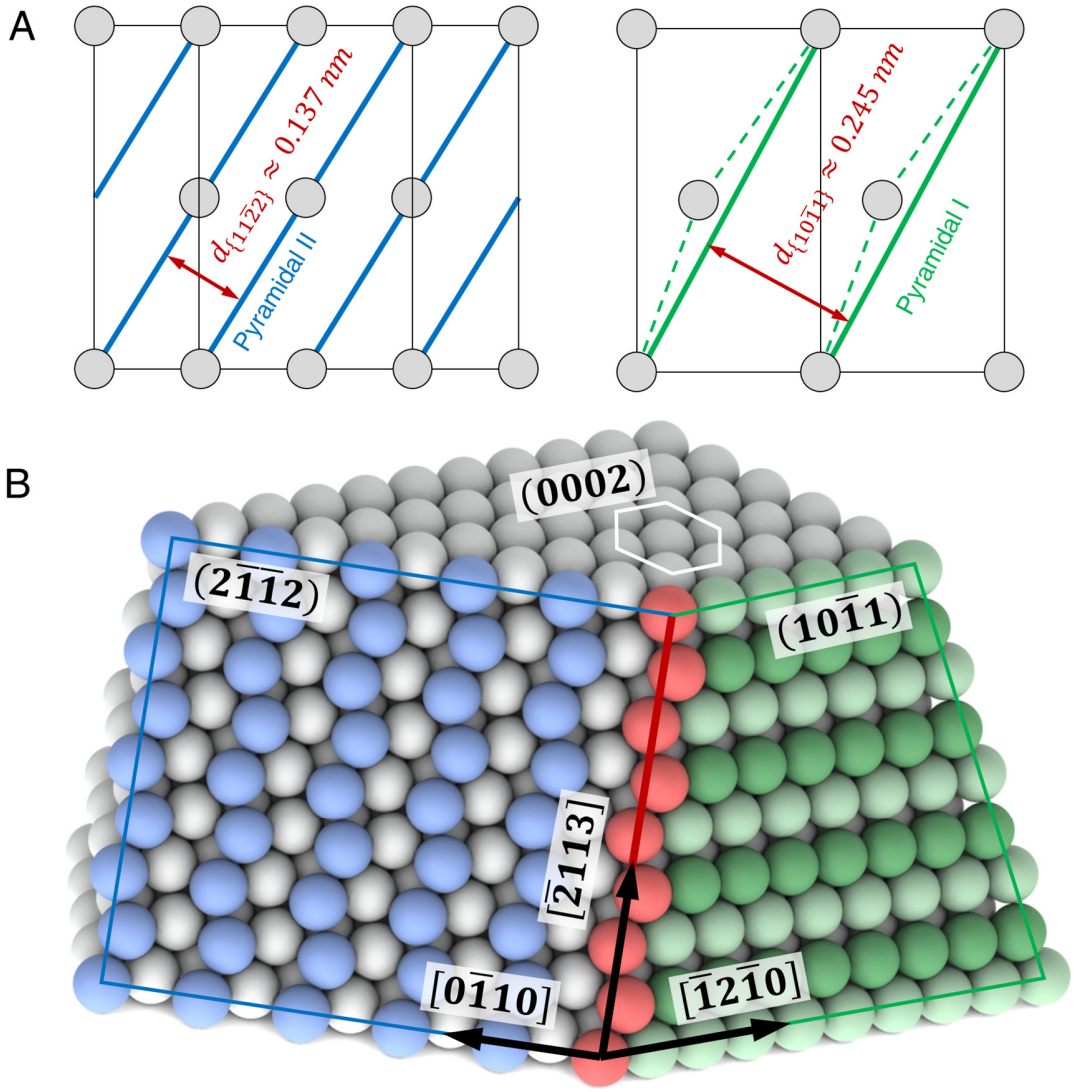

Fig. S13.

Tilting operation used for 3D image reconstruction. (A) Selected dark-field TEM images obtained at tilting angles of -33°, -20°, -10°, 0°, 10°, 20° and 33°. These images were acquired under the two-beam condition $\boldsymbol{g} = (0002)$. (B) Magnified image of the area (yellow dashed frame in A) showing the dislocations for 3D image reconstruction. The positions of dislocations 1, 2 and 3 are marked by blue, red and green dots, respectively. The segments near pillar surface (marked by yellow dashed frames) are blurry in many other images and cannot be successfully reconstructed, thus not displayed in Fig. 4.

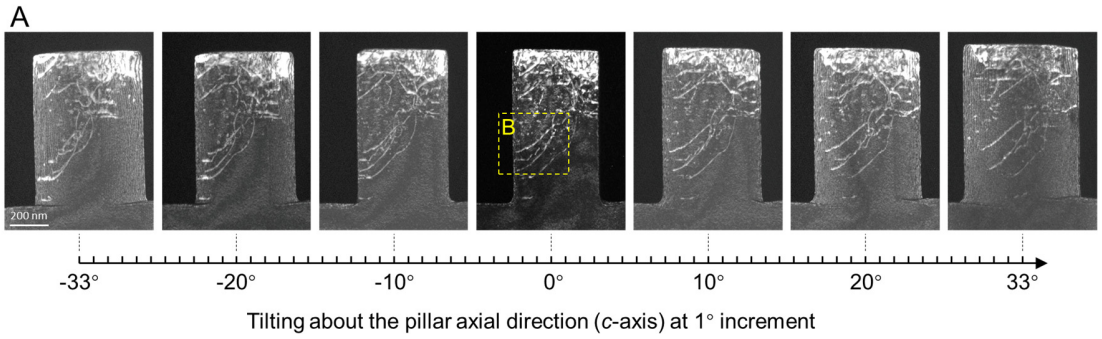

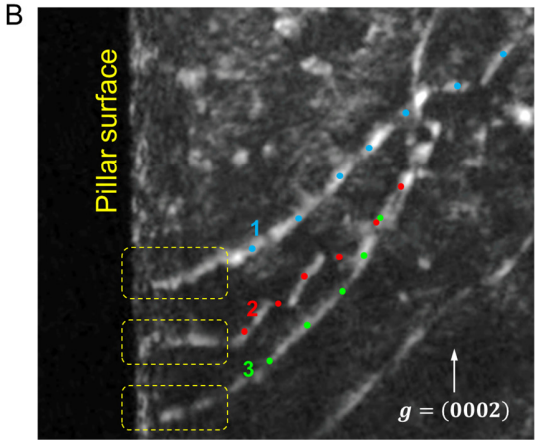

Table S1.

Size and mechanical properties of pillars. Definitions of pillar width, thickness and height are illustrated in fig. S4. Engineering stress is calculated by $\frac{force}{width \times thickness}$. Engineering strain is calculated by $\frac{Height\ reduction}{Initial\ height}$. Note that no pillar fractured, i.e. the value of plastic strain is not the fracture strain, but rather the strain at which the test was terminated. Higher plastic strain values would be obtained if the test continued. The compression test was terminated due to one of the following reasons: (1) automatic termination when the programmed straining was finished, or (2) manual termination to obtain quality images of dislocations.

#	Width × Thickness / nm^2	Height / nm	Yield stress / GPa	Plastic strain
1	475×510	1110	0.68	8%
2	434×443	820	0.76	25%
3	443×458	860	0.60	24%
4	448×453	860	0.75	31%
5	431×436	860	0.74	18%
6	443×412	870	0.63	21%
7	439×422	870	0.61	13%
8	431×456	860	0.67	23%
9	977×1076	2000	0.33	13%
10	1054×1100	2018	0.50	9%
11	398×399	813	0.77	12%
12	436×436	844	0.67	13%
13	397×397	833	0.94	12%
14	428×461	842	0.62	26%
15	407×439	811	0.81	10%

Movie S1.

In-situ TEM compression on a Mg pillar. Mechanical data is displayed next to the movie (Fig. 1 is from this movie).

Movie S2.

In-situ TEM compression of a Mg sample with a trapezoidal shape. The white frame marks the area of interest (Fig. 2 is from this movie).

Movie S3.

In-situ TEM compression of a Mg pillar showing the expansion of a dislocation half-loop (Fig. 3A and fig. S6 are from this movie).

Movie S4.

In-situ TEM compression of a Mg pillar showing the glide of an edge segment of a dislocation in the root area just below the pillar (Fig. 3B is from this movie).

Movie S5.

In-situ TEM compression of a Mg pillar. Area-A corresponds to fig. S7. Area-B corresponds to Fig. 3C. Magnified Area-A and -B are displayed at right.

Movie S6.

In-situ TEM compression of a Mg pillar. Area A corresponds to fig. S8. Magnified Area-A is displayed at right.

Movie S7.

Molecular dynamics simulation of dislocations generated under *c*-axis compression (fig. S9 is from this movie).

Movie S8.

A movie made by 67 TEM images acquired from a series of tilting angles (-33° to +33°) at 1° increment (fig. S13 is from this movie).

Movie S9.

Reconstructed dislocations that are displayed by UCSF-Chimera software (Fig. 4 is from this movie).

References and Notes

1. T. M. Pollock, Weight loss with magnesium alloys. *Science* **328**, 986–987 (2010). doi:10.1126/science.1182848 Medline

2. M. H. Yoo, Slip, twinning, and fracture in hexagonal close-packed metals. *Metall. Mater. Trans. A* **12**, 409–418 (1981). doi:10.1007/BF02648537

3. S. Agnew, D. Brown, C. Tome, Validating a polycrystal model for the elastoplastic response of magnesium alloy AZ31 using in situ neutron diffraction. *Acta Mater.* **54**, 4841–4852 (2006). doi:10.1016/j.actamat.2006.06.020

4. S. Sandlöbes, M. Friák, S. Zaefferer, A. Dick, S. Yi, D. Letzig, Z. Pei, L.-F. Zhu, J. Neugebauer, D. Raabe, The relation between ductility and stacking fault energies in Mg and Mg–Y alloys. *Acta Mater.* **60**, 3011–3021 (2012). doi:10.1016/j.actamat.2012.02.006

5. S. Sandlöbes, Z. Pei, M. Friák, L.-F. Zhu, F. Wang, S. Zaefferer, D. Raabe, J. Neugebauer, Ductility improvement of Mg alloys by solid solution: Ab initio modeling, synthesis and mechanical properties. *Acta Mater.* **70**, 92–104 (2014). doi:10.1016/j.actamat.2014.02.011

6. S. R. Agnew, L. Capolungo, C. A. Calhoun, Connections between the basal I1 “growth” fault and <c+a> dislocations. *Acta Mater.* **82**, 255–265 (2015). doi:10.1016/j.actamat.2014.07.056

7. S. Sandlöbes, M. Friák, S. Korte-Kerzel, Z. Pei, J. Neugebauer, D. Raabe, A rare-earth free magnesium alloy with improved intrinsic ductility. *Sci. Rep.* **7**, 10458 (2017). doi:10.1038/s41598-017-10384-0 Medline

8. Z. Wu, W. A. Curtin, The origins of high hardening and low ductility in magnesium. *Nature* **526**, 62–67 (2015). doi:10.1038/nature15364 Medline

9. Z. Wu, W. A. Curtin, Intrinsic structural transitions of the pyramidal I <c+a> dislocation in magnesium. *Scr. Mater.* **116**, 104–107 (2016). doi:10.1016/j.scriptamat.2016.01.041

10. R. Ahmad, Z. Wu, S. Groh, W. A. Curtin, Pyramidal II to basal transformation of <+> edge dislocations in Mg-Y alloys. *Scr. Mater.* **155**, 114–118 (2018). doi:10.1016/j.scriptamat.2018.06.026

11. Z. Wu, R. Ahmad, B. Yin, S. Sandlöbes, W. A. Curtin, Mechanistic origin and prediction of enhanced ductility in magnesium alloys. *Science* **359**, 447–452 (2018). doi:10.1126/science.aap8716 Medline

12. Y. Tang, J. A. El-Awady, Formation and slip of pyramidal dislocations in hexagonal close-packed magnesium single crystals. *Acta Mater.* **71**, 319–332 (2014). doi:10.1016/j.actamat.2014.03.022

13. A. Kumar, B. M. Morrow, R. J. McCabe, I. J. Beyerlein, An atomic-scale modeling and experimental study of <c+a> dislocations in Mg. *Mater. Sci. Eng. A* **695**, 270–278 (2017). doi:10.1016/j.msea.2017.04.027

14. Z. Ding, W. Liu, H. Sun, S. Li, D. Zhang, Y. Zhao, E. J. Lavernia, Y. Zhu, Origins and dissociation of pyramidal <c+a> dislocations in magnesium and its alloys. *Acta Mater.* **146**, 265–272 (2018). doi:10.1016/j.actamat.2017.12.049

15. H. Fan, J. A. El-Awady, Towards resolving the anonymity of pyramidal slip in magnesium. *Mater. Sci. Eng. A* **644**, 318–324 (2015). doi:10.1016/j.msea.2015.07.080

16. K. Y. Xie, Z. Alam, A. Caffee, K. J. Hemker, Pyramidal I slip in c-axis compressed Mg single crystals. *Scr. Mater.* **112**, 75–78 (2016). doi:10.1016/j.scriptamat.2015.09.016

17. B. Y. Liu, J. Wang, B. Li, L. Lu, X.-Y. Zhang, Z.-W. Shan, J. Li, C.-L. Jia, J. Sun, E. Ma, Twinning-like lattice reorientation without a crystallographic twinning plane. *Nat. Commun.* **5**, 3297 (2014). doi:10.1038/ncomms4297 Medline

18. B.-Y. Liu, N. Yang, J. Wang, M. Barnett, Y.-C. Xin, D. Wu, R.-L. Xin, B. Li, R. L. Narayan, J.-F. Nie, J. Li, E. Ma, Z.-W. Shan, Insight from in situ microscopy into which precipitate morphology can enable high strength in magnesium alloys. *J. Mater. Sci. Technol.* **34**, 1061–1066 (2018). doi:10.1016/j.jmst.2018.01.017

19. Materials and methods are available as supplementary materials.

20. T. Obara, H. Yoshinga, S. Morozumi, $\{11\bar{2}2\}\langle\bar{1}\bar{1}23\rangle$ slip system in magnesium. *Acta Metall.* **21**, 845–853 (1973). doi:10.1016/0001-6160(73)90141-7

21. J. Geng, M. F. Chisholm, R. K. Mishra, K. S. Kumar, An electron microscopy study of dislocation structures in Mg single crystals compressed along [0001] at room temperature. *Philos. Mag.* **95**, 3910–3932 (2015). doi:10.1080/14786435.2015.1108531

22. J. Jain, P. Cizek, K. Hariharan, Transmission electron microscopy investigation on dislocation bands in pure Mg. *Scr. Mater.* **130**, 133–137 (2017). doi:10.1016/j.scriptamat.2016.11.035

23. B. Li, Q. W. Zhang, S. N. Mathaudhu, Basal-pyramidal dislocation lock in deformed magnesium. *Scr. Mater.* **134**, 37–41 (2017). doi:10.1016/j.scriptamat.2017.02.040

24. P. B. Price, Pyramidal glide and the formation and climb of dislocation loops in nearly perfect zinc crystals. *Philos. Mag.* **5**, 873–886 (1960). doi:10.1080/14786436008238307

25. M. Itakura, H. Kaburaki, M. Yamaguchi, T. Tsuru, Novel Cross-Slip Mechanism of Pyramidal Screw Dislocations in Magnesium. *Phys. Rev. Lett.* **116**, 225501 (2016). doi:10.1103/PhysRevLett.116.225501 Medline

26. C. M. Byer, B. Li, B. Cao, K. T. Ramesh, Microcompression of single-crystal magnesium. *Scr. Mater.* **62**, 536–539 (2010). doi:10.1016/j.scriptamat.2009.12.017

27. M. R. Barnett, Twinning and the ductility of magnesium alloys. *Mater. Sci. Eng. A* **464**, 8–16 (2007). doi:10.1016/j.msea.2007.02.109

28. J. R. Kremer, D. N. Mastronarde, J. R. McIntosh, Computer visualization of three-dimensional image data using IMOD. *J. Struct. Biol.* **116**, 71–76 (1996). doi:10.1006/jsbi.1996.0013 Medline

29. E. F. Pettersen, T. D. Goddard, C. C. Huang, G. S. Couch, D. M. Greenblatt, E. C. Meng, T. E. Ferrin, UCSF Chimera—A visualization system for exploratory research and analysis. *J. Comput. Chem.* **25**, 1605–1612 (2004). doi:10.1002/jcc.20084 Medline

30. X. Y. Liu, J. B. Adams, F. Ercolessi, J. A. Moriarty, EAM potential for magnesium from quantum mechanical forces. *Model. Simul. Mater. Sci. Eng.* **4**, 293–303 (1996). doi:10.1088/0965-0393/4/3/004

31. D. Y. Sun, M. I. Mendelev, C. A. Becker, K. Kudin, Tomorr Haxhimali, M. Asta, J. J. Hoyt, A. Karma, D. J. Srolovitz, Crystal-melt interfacial free energies in hcp metals: A molecular dynamics study of Mg. *Phys. Rev. B* **73**, 024116 (2006). doi:10.1103/PhysRevB.73.024116

32. R. W. Hertzberg, R. P. Vinci, J. L. Hertzberg, *Deformation and Fracture Mechanics of Engineering Materials* (Wiley, ed. 5, 2012).